USE OF IR IMAGING TO STUDY EVOLUTION AND PROPAGATION OF THE GROUND FOREST FIRES

A.M. Grishin, A.A. Dolgov, V.P. Zima, V.V. Reino, and R.Sh. Tsvyk

Tomsk State University,
Institute of Atmospheric Optics,
Siberian Branch of the Russian Academy of Sciences, Tomsk
Received June 4, 1997

We present some results of using IR imaging to study the dynamics of brightness temperature field of the ground forest fires from linear and point fire sources under laboratory conditions. Dynamics of some characteristics (speed of fire front propagation, size of flaming zone, total energy, etc.) and time variation of the brightness temperature field are analyzed. Empirical relations between these characteristics and the phase of the fire are derived.

Ground forest fires (GFFs) are most usual in nature and have a tremendous effect on the ecology and economy. Despite of a good deal of experimental work[1-3] devoted to forest fires, the primary mechanism by which the energy is transferred from flaming zone to new combustible material is still uncertain. Neither the exact profiles of concentrations of fire products at the fire front nor the limiting conditions of front propagation are sufficiently well studied. Forest fire detection techniques begin to use passive optical-electronic systems[4,5] onboard satellites. However, to assess the performance of satellite sensors as well as the fire forest identification, classification, and forecasting, one needs to know such characteristics as heat fluxes in specific spectral intervals, radiation attenuation by the atmosphere, smoke particles, and forest canopy, effective burning areas as a function of fire type, and so on. Also, it is important to keep in mind that burning of forest combustible materials (FCMs) depends on their density, wetness, initial temperature, as well as on the ambient air humidity and temperature, wind speed and direction, and local relief inclination. Global study of the GFFs in the field is hindered by poor reproducibility of the results and by high sensitivity of the fire parameters to the ambient conditions. Generally, this difficulty is avoided by using laboratory setups capable of modeling, more or less correctly, the conditions
for onset and development of the ground forest fires. Thus, Refs. 6–8 describe setups for physical modeling of GFFs in special wind tunnels. This technique, however, is unavoidably draw back since the FCM burning in a real open space is modeled as the one in a semiclosed space of experiment. This closing changes temperature and chemical composition in the burning zone and impacts the fire front velocity by altering the draught force in the GFF zone. However, such experimental studies of fires under laboratory conditions are in progress until now.

In the course of these studies, new laboratory setups are created with which a wider range of FCM burning events can be covered and a closer approach to real conditions is achievable. Compared to field studies, the work in laboratory is not limited by season and is less expensive.

MEASUREMENT TECHNIQUE

In Ref. 9 one may find a description of the setup and technique for studying the onset and development of the ground forest fires under model conditions by means of IR imaging. Major advantage of the IR imaging systems is their high spatial and temporal resolution. At present, this method is successively used to study the dynamics of variations in brightness temperature field and to derive some FCM burning characteristics, both quantitative (speed of propagation, fire size, burning phase) and qualitative (relative changes of maximum temperature, total energy, etc.). Obtaining quantitative data on energy and temperature characteristics of burning process must involve measurements of absolute values of the light fluxes and, consequently, IR imager calibration in the 300–1300°C temperature range. In addition, the flame emissivity in different spectral intervals, which is the function of aerosol particle, water vapor, and carbon dioxide concentrations,[10] must be known. This will serve as the data base for developing and refining satellite techniques for detection of fires at their early stages, for assessing their intensity, and for forecasting their evolution.

The model setup[9] includes table-polygon 1.3×0.75 m^2 in size covered with a 0.1-m deep soil layer (upon which was superimposed a portion of studied combustible material), a set of sensors whose outputs were entered to a computer, firing coil of specified configuration (large- or small-size tungsten coil), and IR imaging system AGA-780 (operating in 3–5 μm wavelength region) complemented with a special programmed module Termik-2[11] and an IBM AT computer. Use of the programmed module makes it is possible to monitor dynamics of both the slow- and high-speed processes by skipping out a specified number of images.

0235-6880/97/10 712-08 $02.00 © 1997 Institute of Atmospheric Optics

In this paper we present some results of the experimental study (using a model setup) of the GFFs evolution from a linear and most likely, a point fire source. The IR imager, located at a distance of 6–7 m from the table-polygon, measures thermal radiative flux from each elemental flaming zone (cell). An image is composed of 95×95 (programally specified) flaming cells. The IR imager was elevated about 1.5 m above the plane of the table-polygon, which allowed us to fix the fire front shape and size along each of the coordinate axes (horizontal X and Y in the table plane and vertical Z). For a linear fire source, the IR imager was mounted at the level of the table-polygon; the results obtained are summarized in Ref. 12.

For a point fire source, the results obtained were processed on per image basis to derive the following fire parameters: coordinates X_l and X_r of the left and right edges of the fire front along the horizontal X axis, lower (nearest) Y coordinate (farthest Y coordinate is obscured by the flame and is invisible in the thermograms); the upper coordinate Z of flame height (vertical axis), the relative maximum brightness temperature T_m, parameter P which is proportional to the fire energy release for 0.04 s, and the area of horizontal projection S of the flame. Signal level at which the coordinates T were determined was taken to be 9–20 relative units of brightness temperature, that is about 10% of the maximum value recorded with the IR imager. The coordinate system origin X_0, Y_0, Z_0 was chosen to be at the point of the maximum temperature at the time of the fire onset. Spatial resolution was calibrated by observing heated rectangular plate placed in the polygon table plane. The spatial resolution between two points of an image was found to be 7.7 mm along X and Z axes, and 30.6 mm along Y axis, owing to the IR imager – polygon table geometry. Total record length was 120–240 s, depending on the number of images skipped. Each image was taken for 0.04 s, every 1.2–2.4 s (with every 30–60 images skipped). In experiments with a linear fire source, the vertical and horizontal resolutions were 11.2 mm.

The processing technique was the following. For a point fire source, we determined the coordinates X_l, X_r, and Z from images to calculate the diameters of the fire front ring along x and y axes, $D_x(t)$ and $D_y(t)$, and the flame height $h(t)$ from the formulas: $D_x(t) = X_r(t) - X_l(t)$, $D_y(t) = 2(Y(t) - Y_0)$, and $h(t) = Z(t) - Z_0$. Equations of regression lines for data processing were obtained by rms fitting. Routinely, in each image (of 0.04 s duration) we determined and calculated: the maximum temperature of the flaming zone and its total energy and the area by summing over the flaming area. For a nonlinear, in time process, the approximating equations were chosen by fitting with the account for the physics of the process studied.

MEASUREMENT RESULTS

As a burning material in experiments with a linear fire source, we used dry cedar needles (with humidity $\omega \approx 13\%$ and mass 0.2 kg) organized in a layer of the depth $h \approx 0.02$ m on the surface of the table-polygon (density $\rho \approx 20$ kg/m^3, and content of the burning material $m_3 \approx 0.42$ kg/m^2). With a point fire source, we took dry cedar needles as a burning material (with humidity $\omega \approx 13\%$ and mass 0.185 kg) arranged in a circle-shaped layer of the depth $h \approx 0.04$ m (with the diameter $D = 0.5$ m, density $\rho \approx 23.6$ kg/m^3, and content of the burning material $m_3 \approx 0.9$ kg/m^2). Following the classification in Ref. 13, there has been realized a light ground forest fire.

The burning process evolution was divided into three stages: (1) fire onset and formation of the fire front within the time interval $0 < t < t_1$, (2) steady-state burning $t_1 < t < t_2$, and (3) decay $t_2 < t < t_3$, each characterized by a distinct set of parameters.

We analyzed the shape of the flaming zone, averaged over the burning period, and found it to be significantly different for fires from a point source (Fig. 1*b*) and those from a linear one (Fig. 1*a*).

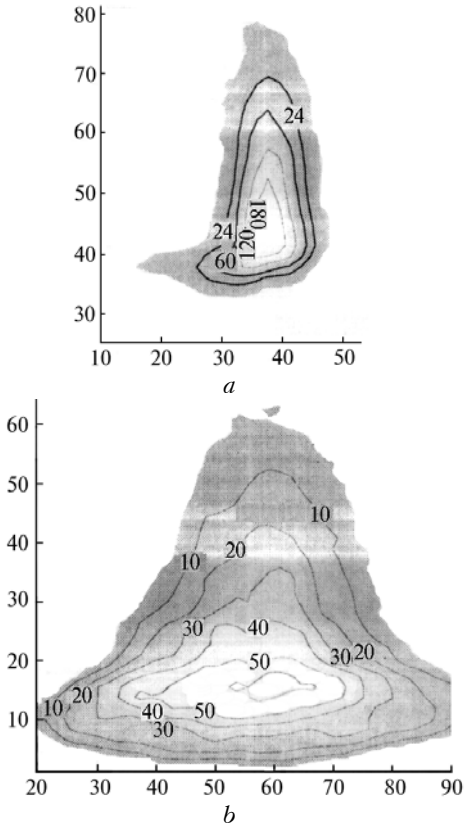

FIG. 1. Average shape of the flaming zone for fires from a linear (a) and a point (b) source.

Coordinate axes in Figs. 1*a* and *b* represent image pixel's numbers. Flaming zone from a linear source is constant with time and shaped as an asymmetric gaussoid.

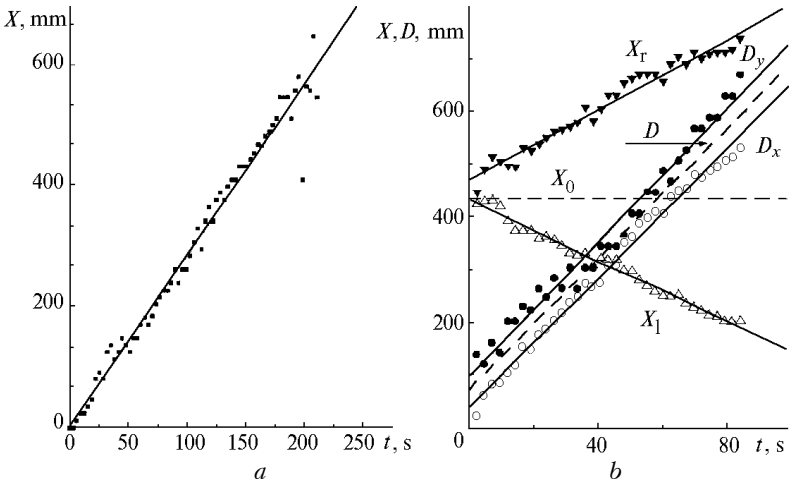

FIG. 2. Fire front propagation: a linear-source (a) and a point source (b) fires.

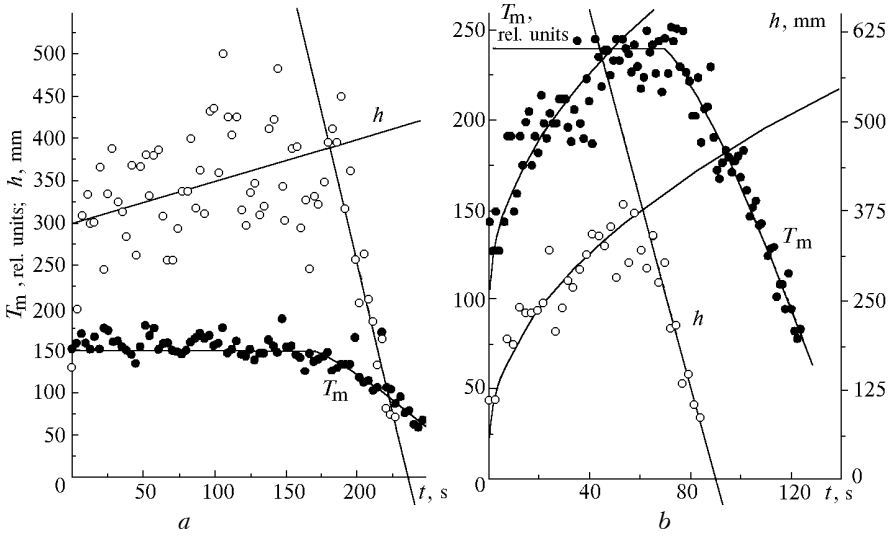

FIG. 3. Time change of flaming zone maximum temperature T_m and flame height h for fires from a linear (a) and a point (b) sources.

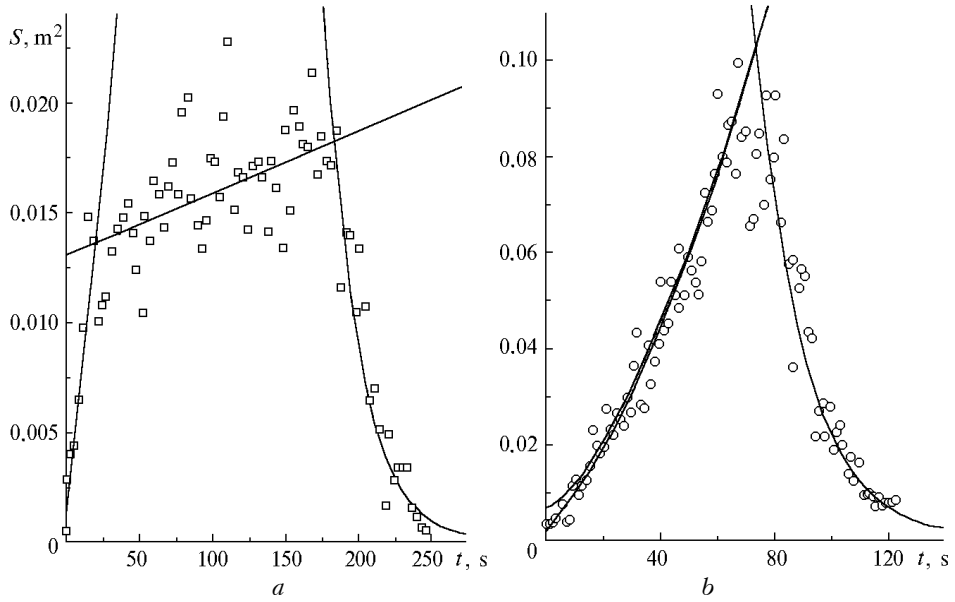

FIG. 4. Time change of the flaming zone area S(t) for fires from a linear (a) and a point (b) sources.

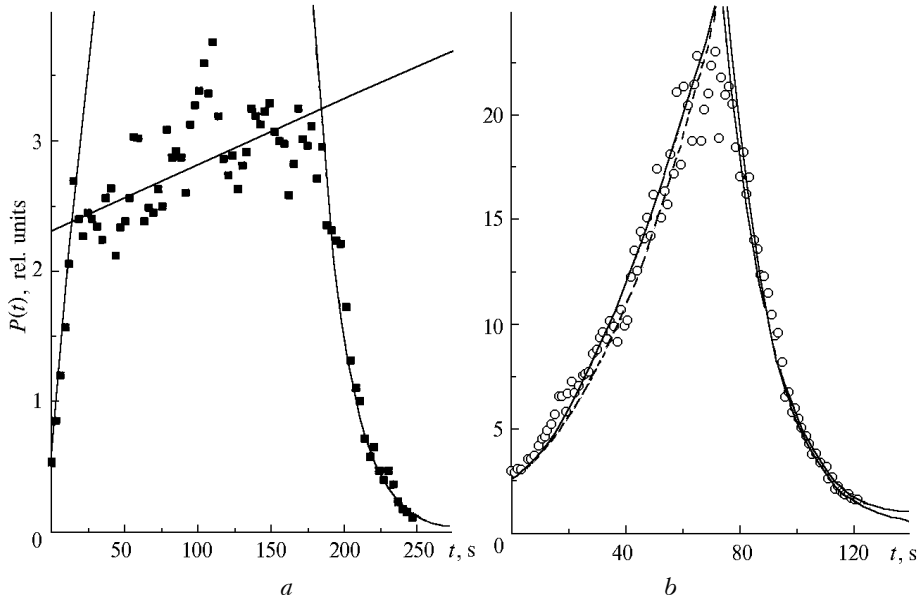

FIG. 5. Time change of the total flame energy P(t) for fires from a linear (a) and a point (b) sources.

Unlike, the flaming zone from a point source first is shaped approximately as a cylinder, during first 60 s of burning then it changes to cone with the bottom radius and height growing with time, then it becomes a truncated cone, and finally (in 100 s, when remainders of the combustible material burn down) a burning ring. The change of flaming zone shape from a cone to a truncated cone coincides in time with the fall off of the fire front propagation velocity (Fig. 2), rate of change of the flame height (stabilization), as well as of maximum temperature (Fig. 3), and flaming zone area (Fig. 4), and its total energy (Fig. 5). The cause of such a shape of the flaming zone may be that, in a ring-shaped fire, the air influx along the external front is larger than that along the internal (inside flaming zone) front, with correspondingly slower burning process inside the flaming zone. In addition, the lack of air, its hot temperature and fast lifting due to buoyancy, cause a decrease of the air pressure inside the flaming zone and contract it to the cone shape. The average front width and total energy[6] changed slightly during the study of the linear fire (except during fire onset and termination); while in the ring-shaped fire, the total energy constantly grew up to the moment when the front reaches the edge of the FCM zone.

Typically burning process is characterized by the front propagation velocity U_f, maximum temperature T_m, flame height h, flaming zone area S, radiative energy P, radiative energy density of the flame W, as well as by fluctuations of these parameters. Below we address those parameters in the order.

FIRE FRONT PROPAGATION VELOCITY

Figure 2,*a* presents time change of X coordinate (in the direction of fire front propagation) of the hottest fire point, X_m, for a point fire source. RMS fitted equation has the form

$$x_m(t) = A + U_f\, t = 2.84\, t. \quad (1)$$

Figure 2,*b* shows, for a point-source fire, an example of time change of X_l and X_r coordinates, of the front diameters along X and Y axes, $D_x(t)$ and $D_y(t)$, as well as the rms diameter $D(t) = \sqrt{[D_x^2(t) + D_y^2(t)]/2}$. Vertical axis represents coordinates and diameters in millimeters, and the horizontal is the time t in seconds; straight lines are plotted by rms fitting using the first-order equation $F(x) = A + U_f t$ where A and U_f are constants that determine the $F(x)$ value at the zero point and the rate of its variation. The best fits are

$$x_l(t) = 431 + 2.82\, t; \quad x_r(t) = 470 + 3.33\, t;$$

$$D_x(t) = 38.8 + 6.15\, t; \quad D_y(t) = 96.7 + 6.38\, t; \quad (2)$$

$$D(t) = A + 2U_f\, t = 73 + 6.2\, t$$

with the correlation coefficient of 0.98–0.99.

As seen from Fig. 2*b* and equation (2), under windless conditions the fire front propagates at a constant speed $U_f = 3.1$ mm/s in all directions, i.e. it is approximately shaped as a circle with the diameter increasing at a rate of 6.2 mm/s. The propagation speed fluctuates with the frequencies higher than 0.05 Hz. The measured fire front speed is 3.1 mm/s, that well agrees with $U_f^c = U_\infty[1 - \exp(-4m_3)] = 3$ mm/s as calculated in Ref. 1 for $U_\infty = 3.6$ mm/s at $m_3 = \infty$, and with $U_f^{tm} = 4$ mm/s measured with a thermocouple. For a linear fire, the front speed is 2.5–3 mm/s.[12] That is, the front speed for fires in the first and second phases depends on the fire source type only weakly, and varies with FCM wetness and wind velocity. In the third phase (decay), the fire front speed vanishes.

FLAME TEMPERATURE AND HEIGHT

The maximum brightness temperature $T_m(t)$ of the flaming zone in relative units and the flame height $h(t)$ in millimeters are plotted in Fig. 3*a* for a linear-source fire and in Fig. 3*b* for a point-source fire versus time t. Curves $T_m(t)$ and $h(t)$ are plotted versus time using the fit $A + b\,t^c$. For a linear-source fire (phase 1 calculation is incomplete):

2nd phase:

$$T_m(t) = 160; \quad h(t) = 325 + 0.5\,t \quad \text{for } t_1 < t < t_2\,, \quad (3)$$

3rd phase:

$$T_m(t) = 160 - 0.47\,(t - 0.9t_2)^{1.24};$$

$$h(t) = 325 - 7\,(t - t_2) \quad \text{for } t > t_2 \approx 180 \text{ s}. \quad (4)$$

For a point-source fire (phase 2 calculation is incomplete):

1st phase:

$$T_m(t) = 100 + 20\sqrt{t};$$

$$h(t) = 45 + 42.5\sqrt{t} \quad \text{for } t < t_1 \approx 60 \text{ s}\,, \quad (5)$$

3rd phase:

$$T_m(t) = 240 - (t - t_2)^{1.24};$$

$$h(t) = 280 - 13\,(t - 0.9\,t_2) \quad \text{for } t > t_2 \approx 75 \text{ s}, \quad (6)$$

where t_2 is the time when the fire front reaches the edge of the FCM zone, which is determined from fire images and fire front speed.

For a linear-source fire, the flame height for needle fall ($k = 9$) was calculated using empirical formula from Ref. 1 to be $h = k\sqrt{m_3\,U_f} = 0.475$ m, that is somewhat higher than that obtained in this experiment.

From Figs. 3*a*,*b*, we see that the phase 1 fires not having reached establishment stage have variations of the flame temperature and height that strongly depend on source type. The flame temperature and height increase rapidly (for 5–15 s) and linearly for a linear fire source, while growing nonlinearly, as $t^{1/2}$ (for 50 s), for its point counterpart.

In the second phase, the flame height and maximum temperature stabilize. For a linear-source fire, the average flame height increases a little bit (at least for a source strip ~0.7 m in length), while the average maximum temperature is fairly constant with time. In the point-source fire, the smallness of flaming zone has made it possible to observe second phase for 15–20 s only.

Phase 3 (decay) does not depend on fire source type. During it, the flame height decreases as $(t - t_2)$, while the maximum temperature as $(t - t_2)^{1.24}$. However, the decay rate is lower in the linear than in the point fire. The constants A in this phase correspond to the maximum average value of parameters T_m and h_m recorded early in the phase.

SIDE-VIEW AREA OF THE FLAMING ZONE

Figure 4*a*,*b* presents variations of the area of the flaming zone, that emits in the direction of IR imager (half of the flaming zone area), determined at the ~$0.1T_m$ level. Approximate curves of time dependence are obtained by rms fitting.

For the linear-source fire:

1st phase:

$$S(t) = 0.001 + 0.0006\,t \quad \text{for} \quad t < t_1 \approx 20 \text{ s}\,, \quad (7)$$

2nd phase:

$$S(t) = 0.013 + 0.000028\,t \quad \text{for} \quad t_1 < t < t_2 \approx 185 \text{ s}\,, \quad (8)$$

3rd phase:

$$S(t) = S_m \exp\left[-\frac{t - t_2}{t_m}\right] = 0.018 \exp\left[-\frac{t - 185}{22}\right]$$

$$\text{for} \quad t > t_2 \approx 185 \text{ s}. \quad (9)$$

For the point-source fire:

1st phase:

$$S(t) = 0.5\,\frac{\pi}{2}\,\frac{D(t)}{2}\sqrt{\left(\frac{D(t)}{2}\right)^2 + (h(t))^2}$$

$$\text{for} \quad t < t_1 \approx 70 \text{ s}. \quad (10)$$

3rd phase:

$$S(t) = S_m \exp\left[-\frac{t - t_2}{t_m}\right] = 0.09 \exp\left[-\frac{t - 75}{22}\right]$$

$$\text{for} \quad t > t_2 \approx 75 \text{ s}. \quad (11)$$

Equation (10) describes $S(t)$ dependence during the phases of fire onset and fire front formation, from firing to the time the fire front comes close to the external edge of the FCM zone (70–80 s into the burning). This is taken as a half-area of the cone side (based on the flame shape), i.e. $S(t) = A\,(\pi/2)\,R(t)\,L(t)$, where A is the fitting parameter, $R(t) = D(t)/2$ is the radius of the cone base, $L(t) = \sqrt{\left(\frac{D(t)}{2}\right)^2 + (h(t))^2}$ is the length of the cone slope, while $D(t)$ and $h(t)$ dependences are derived experimentally (see Eqs. (2) and (5)).

Equations (9) and (11) govern the decay phase of the burning process associated with the front arrival at the FCM zone edge and burning down of the FCM remainders. These equations are derived by trial and error method, assuming exponential decay driven by the following parameters: maximum average area of the flaming zone S_m, constant t_m determining the decay rate, and time t_2 of the onset of the decay phase. As the figures show, the above equations fit experimental data pretty well.

Instead of the equation (10), simpler relation, $S(t) = 0.07 + (0.0028t)^{3/2}$, can be used to describe the first phase of a point-source fire, which well fits the experimental results in the phases of the fire onset and front formation.

TOTAL ENERGY

Shown in Fig. 5*a* for linear source and in Fig. 5*b* for point source is the dependence of a quantity proportional to the time change, over 0.04 s, of the flame total energy $P(t)$ on per image basis. Time fits are the following.

For the linear-source fire:

1st phase:

$$P(t) = 0.54 + 0.123\, t \quad \text{for} \quad t < t_1 \approx 20 \text{ s}, \tag{12}$$

2nd phase:

$$P(t) = 2.3 + 0.005\, t \quad \text{for} \quad t_1 < t < t_2 \approx 185 \text{ s}, \tag{13}$$

3rd phase:

$$P(t) = P_m \exp\left[-\frac{t - t_2}{t_m}\right] = 3 \exp\left[-\frac{t - t_2}{20}\right]$$

$$\text{for} \quad t > t_2 \approx 185 \text{ s}. \tag{14}$$

For the point-source fire:

1st phase for $t < t_1 \sim 75$ s:

$$P(t) = 1 + 1.3\, T_m(t)\, S(t) = 1 + 1.3\,(100 + 20\sqrt{t}) \times$$

$$\times 0.5\frac{\pi}{2} 10^{-6} \left(\frac{75 + 6.2t}{2}\right) \sqrt{\left(\frac{73 + 6.2t}{2}\right)^2 + (45 + 42.5\sqrt{t})^2}; \tag{15}$$

$$P(t) = 2.1 + 0.075\, t + 0.55\,(100 + 20\sqrt{t}) \times$$

$$\times 0.5\frac{\pi}{2} 10^{-6} \left(\frac{75 + 6.2t}{2}\right) \sqrt{\left(\frac{73 + 6.2t}{2}\right)^2 + (45 + 42.5\sqrt{t})^2}; \tag{16}$$

3rd phase for $t > t_2 = 75$ s:

$$P(t) = 2.4 + 0.852\, T_m(t)\, S(t) =$$

$$= 2.4 + 0.85\,(240 - (t - t_2))^{1.24} 0.1 \exp\left[-\frac{t - 75}{17}\right]. \tag{17}$$

Still remaining good fits to experimental data, equations (15) and (17) may be simplified to read

1st phase:

$$P(t) = P_m + (0.11\, t)^{3/2} \quad \text{for } t < t_1 = 75 \text{ s}, \tag{18}$$

3rd phase:

$$P(t) = P_m \exp\left[-\frac{t - t_2}{t_m}\right] = 25 \exp\left[-\frac{t - t_2}{17}\right]$$

$$\text{for } t > t_2 = 75 \text{ s}. \tag{19}$$

Equation (15) describes $P(t)$ dependence during the phases of the fire onset and fire front formation, from firing to the time the fire front comes close to the external edge of the FCM zone (75–80 s into the burning). This is taken as the cone side area in this burning phase $S(t)$ (Eq. (10)) times the maximum temperature $T_m(t)$ (Eq. (5)). The offset 1 and the slope of 1.3 are chosen to give the best fit to the experimental data; a better fit to the experimental data in this burning phase, Eq. (16), is modified from Eq. (15) by including an extra term $0.0075t$ accounting for the energy variation during the early burning phase.

Equation (17) describes the decay phase of the burning process associated with the front arrival at the FCM zone edge and burning down of the FCM remainder. Again, it is obtained as the product of the maximum temperature $T_m(t)$ and the flaming zone area $S(t)$ in this burning phase. Constant factors and terms are adjusted to give the best fit to the experimental data.

As seen from the figures and equations, the total energy in the first burning phase depends on the fire source shape; it is directly proportional to time for a linear source, while scaling as $t^{3/2}$ for its point counterpart. The second phase is characterized by a slow energy growth in the case of a linear-source fire, while being only in its beginning between 60 and 80 s for a point-source one. In the decay phase, the total energy decreases exponentially with time for both source types.

DISCUSSION OF RESULTS

From the combined analysis of the results of processing evolution characteristics of a ground forest fires it can be concluded that

1) The speed of propagation of the external front of burning needle fall under calm conditions is equal to $U_f \sim 3.1$ mm/s in all directions, that well agrees with the value calculated from the formula $U_f^c = U_\infty [1 - \exp(-4\, m)] = 3$ mm/s and only slightly depends on the fire source shape. The point-

source fire front is shaped approximately as a circle with the diameter $D = U_f t$.

2) It is typical for the first phase (during fire onset and front formation, $t < t_1$) that rather a rapid increase in maximum temperature $T_m(t)$, flame height $h(t)$, flaming zone area $S(t)$ and energy $P(t)$, takes place between 10 to 15 s for a linear source and 40 to 50 s for a point source. In addition, the rate of change of these parameters depends on the fire source type.

It is characteristic of a linear fire source, the directly proportional time dependence of the form $T_m(t)$, $h(t)$, $S(t)$, $P(t) \sim A + b t$; while the average fire front shape may be approximated with a cylinder during few first seconds of burning, and with an asymmetric gaussoid with a steeper external front afterward.

For a point source, it is characteristic a less steep nonlinear increase of the maximum temperature and flame height ($T(t)$, $m(t) \sim A + b t^{1/2}$) and a faster growth of the flaming zone area and emitted energy ($S(T)$, $P(t) \sim A + b t^{3/2}$), while the average shape of the flaming zone is initially a cylinder, and then it takes a cone-like surface or a paraboloid of rotation. Physically, such a flaming zone shape is well explained by the burning processes. As the flaming zone increases in size, progressively less oxygen-rich air can access the zone interior, so the fire process slows down there, which might have resulted in the fire front broadening relative to the width of a linear counterpart. Moreover, air temperature and, hence, ascent due to the buoyancy both increase when moving from the flaming zone edge to its center, with ensuing negative pressure gradient in the same direction and flame contraction to the cone. The flaming zone area and the heat release both rapidly (nonlinearly) increase with time.

3) The second-phase fire is a developed process ($t_1 < t < t_2$) which is characterized by a relatively steady burning parameters. For a point-source fire, this is the stage when FCM has burnt over a sufficiently extended area around the flaming zone center; so that pressure at the center restores to its original high value, and the flaming zone changes to a ring shape. At the stage of burning ring the flame height and fire front width must be the same for both types of fire sources. However, for the point-source fire, the flaming zone area will increase linearly with time (front radius) as $S(t) \approx A\ 2\pi\ R(t)\ h(t) = A\ 2\pi\ U_f\ t\ h(t)$, while the total energy nonlinearly as $P(t) \approx A\ 2\pi\ [R_e(t)^2 - R_{in}(t)^2]\ h(t)$, where $R_e(t)$ and $R_{in}(t)$ are the external and internal radii of the fire front. In our experiment, only phase 2 onset was recorded (from 55 to 75 s into the fire), when the maximum temperature and flame height only began to stabilize (Fig. 2*b*), while the area and energy increased linearly with time (Figs. 3*b*, and 4*b*).

4) The third phase, that is the decay ($t > t_2$), e.g., due to depletion of FCM, changes little between the fire source types and is characterized by a rapid decrease of the maximum temperature, flame height, flaming zone area, and energy release. During this, the flame height decreases linearly with time as $h(t) \approx h_m - b(t - t_2)$, the maximum temperature behaves as $T_m(t) \approx T_m - B\ (t - t_2)^{1.24}$, while the flaming zone area and total energy fall off exponentially as $S(t) \approx S_m \exp\left(-\frac{t - t_2}{t_m}\right)$; $P(t) \approx P_m \exp\left(-\frac{t - t_2}{t_m}\right)$, where h_m, T_m, S_m, and P_m are the mean maximum parameter values prior to the fire decay phase, and B and t_m are constants determining the fire decay rate which are likely to be the functions of FCM burning properties.

5) All parameters of burning process fluctuate in time at a minimum frequency about 0.07–0.04 Hz (15–25 s).

ACKNOWLEDGMENT

The present work is supported by the Russian Foundation for Basic Research (grant No. 96–01–00011).

REFERENCES

1. A.M. Grishin, *Mathematical Simulation of Forest Fires and New Techniques of Fire-Fighting* (Nauka, Novosibirsk, 1992), 408 pp.
2. A.M. Grishin, *Physics of Forest Fires* (State University, Tomsk, 1994), 218 pp.
3. E.V. Konev, *Physical Foundations of Vegetable Material Burning* (Nauka, Novosibirsk, 1992), 239 pp.
4. L.A. Mirzoeva, G.B. Kameshkov, E.A. Lustberg, G.A. Makovtsev, and V.F. Zakharenkov, Opticheskii Zhurnal, No. 8, 17–21 (1992).
5. O.Yu. Aksenov, A.I. Antonets, and S.I. Gushchin, Opticheskii Zhurnal, No. 8, 21–23 (1992).
6. R.C. Rothermell, *Airflow characteristics-wind tunnels and combustion facilities at northern forest fire laboratory.* Intermountain Forest and Range Experiment Station Forest Service U.S. Department of Agriculture, Northern Forest Fire Laboratory, Missoula, Montana, 1967.
7. D.R. Weise, in: *Proc. 12th Int. Conf. of Fire and Forest Meteorology* (Jekyll Issland, Georgia, 1993), pp. 572–578.
8. D.R. Weise, "Modeling wind and slope-induced wildland fire behavior," Doct. Phylosophy Dissert., University of California at Bereley (1993).
9. A.M. Grishin and V.P. Zima, in: *Proc. International Simp.-Seminar. Adjacent Problems in Physical Mechanics and the Ecology* (Tomsk, 1994).
10. L.Z. Kriksunov, *Handbook of Essentials of IR Imagery* (Sov. Radio, Moscow, 1978), 300 pp.
11. A.A. Dobrotkin, A.V. Isakov, A.B. Il'in, A.G. Petrenko, V.V. Reino, R.Sh. Tsvyk, and M.V. Sherstobitov, Atmos. Oceanic Opt. **7**, No. 5, 355–357 (1994).
12. A.M. Grishin, A.A. Dolgov, V.P. Zima, A.V. Isakov, V.V. Reino, and R.Sh. Tsvyk, Fiz. Goreniya i Vzryva **6**, No. 6, 3–11 (1996).
13. *Instructions for Forest Fire Detection and Extinguishing* (Gosleskhoz, Moscow, 1976), 110 pp.